Combined DIC and FEA method for analysing debonding crack propagation in fatigue experiments on wrapped composite joints

Feng, Weikang; He, Pei; Pavlovic, Marko

DOI
10.1016/j.compstruct.2022.115977

Publication date
2022

Document Version
Final published version

Published in
Composite Structures

Composite Structures 297 (2022) 115977

Contents lists available at ScienceDirect

Composite Structures

journal homepage: www.elsevier.com/locate/compstruct

Combined DIC and FEA method for analysing debonding crack propagation in fatigue experiments on wrapped composite joints

Weikang Feng, Pei He, Marko Pavlovic *

Faculty of Civil Engineering and Geoscience, Delft University of Technology, 2600AA Delft, the Netherlands

ARTICLE INFO

Keywords:
Wrapped composite joint
Fatigue debonding
CHS
3D DIC
Finite element analysis
Strain energy release rate

ABSTRACT

Wrapped composite joint is a novel joining technology which connects steel hollow sections through bonding, completely avoiding the welding in the load transferring mechanism. Fatigue performance of wrapped joints has been experimentally shown to be superior over their welded counterparts. Aiming to enable development of prediction methods for fatigue life of wrapped composite joints, this paper proposes a combination of 3D Digital Image Correlation (DIC) technique and FE analysis as a method for monitoring debonding crack propagation at a complex composite-to-steel interface covered by a non-uniform thickness laminate. Fatigue tests on wrapped composite X-joints under tensile load are used for the method application and to analyse crack propagation in the brace and chord, including their interaction. Variation of strain distribution on surface of composite wrap obtained in DIC is corelated to length of the debonding crack at the composite-to-steel interface by the means of 3D finite element model of such joint. Crack development obtained from the combined DIC and FEA method is correlated to strain energy release rates calculated from FEA. With the help of FEA, the failure mode is characterised by debonding on the chord at the early stage of cyclic loading, followed by debonding on the brace.

1. Introduction

Fatigue failure has been proved to be a common hazard for welded tubular joints, which are now widely used for circular hollow sections (CHS) of steel truss/jacket supporting structures of off-shore wind turbines, oil and gas platforms, steel bridges [1]. Fatigue-driven design of such structures usually leads to thick profiles and refined welding procedures, which makes application of such structures less cost-effective. In recent years, fiber-reinforced polymers (FRP) have been widely used for enhancing static/fatigue performance of steel structures, especially tubular joints, due to their light weight, tailorability, high fatigue endurance and other excellent mechanical properties [2]. Until now, much experimental work has been conducted and design theories established, showing effectiveness of a such technique on strengthening mechanical behaviour of different kinds of welded steel structures [3–7]. However, most of existing study is only focused on welded joints externally strengthened with composites. The problem of fatigue failure resulting from stress concentration and reduced fracture toughness around weld remains unsolved.

Another technique, proposed by the authors [8], is wrapped composite joint, where a composite wrap is used to connect steel members of hollow sections through bonding and welding is completely avoided in the load transferring mechanism, so that fatigue failure, originating from welding, is eliminated. The concept of wrapped composite joint is shown in Fig. 1. Static [9] and fatigue [10] experiments on this kind of novel composite joints have shown their superior mechanical performance over their welded counterparts. Their fatigue life is even proved to be extended to 10–100 times longer under the same stress range.

Although superior fatigue performance of wrapped composite joints has been confirmed experimentally, there are remaining issues to be solved. One critical issue is monitoring the most important failure mode of the joint wrapped with thick laminates, debonding at the steel-to-composite interface [10], which is of great importance for characterizing and predicting fatigue behaviour of wrapped composite joints. Many researchers have proposed to monitor debonding propagation at the interface by tracing strain development in the composite material on top of the interface. For example, Kentaro [11] and Xinzhe Min [12] used strain gauges to measure strain distribution on surface of FRP to monitor debonding at FRP-concrete interface under fatigue loading. The results showed that the longitudinal strain kept a constant high value at the fully debonded zone, decreasing gradually at the stress transfer zone and with low values at the bonded zone. The length of the plateau with high-stress level increased with number of cycles and was employed as

* Corresponding author.
E-mail address: M.Pavlovic@tudelft.nl (M. Pavlovic).

https://doi.org/10.1016/j.compstruct.2022.115977
Received 28 March 2022; Received in revised form 26 June 2022; Accepted 6 July 2022
Available online 9 July 2022

Nomenclature

CHS	circular hollow section
FRP	fiber reinforced polymer
GFRP	glass fiber reinforced polymer
NDT	non-destructive technique
DIC	digital image correlation
F_{max}	the maximum load
F_{min}	the mimimum load
ΔL_{maxax}	the maximum elongation
ΔL_{min}	the mimimum elongation
N	number of cycles
k	secant stiffness of the joint
FEA	secant stiffness of the joint
LEFM	linear elastic fracture mechanics
E	young's modulus
G	shear modulus
ν	Poisson's ratio
VCCT	virtual crack closure technique
SERR	strain energy release rate
$G_{I/II/III}$	mode I/II/III atrainenergy release rate
$G_{Ic/IIc/IIIc}$	critical mode I/II/III atrainenergy release rate
G_{eq}	equivalent strain energy release rate
$\Delta G_{tot.(max)}$	(the maximum) total strain energy release rate range
η	Benzeggagh–Kenane law parameter
RP	reference point
$l_{b.(max)}$	(the maximum) crack length on the brace
$l_{c.(max)}$	(the maximum) crack length on the chord
α	parameter for defining relationship between l_c and l_b
β	angle between crack front on the brace and axis of brace
y_k	test results
$\bar{y}_k$	mean value of test results
$\hat{y}_k$	predicted results
R^2	coefficient of determination

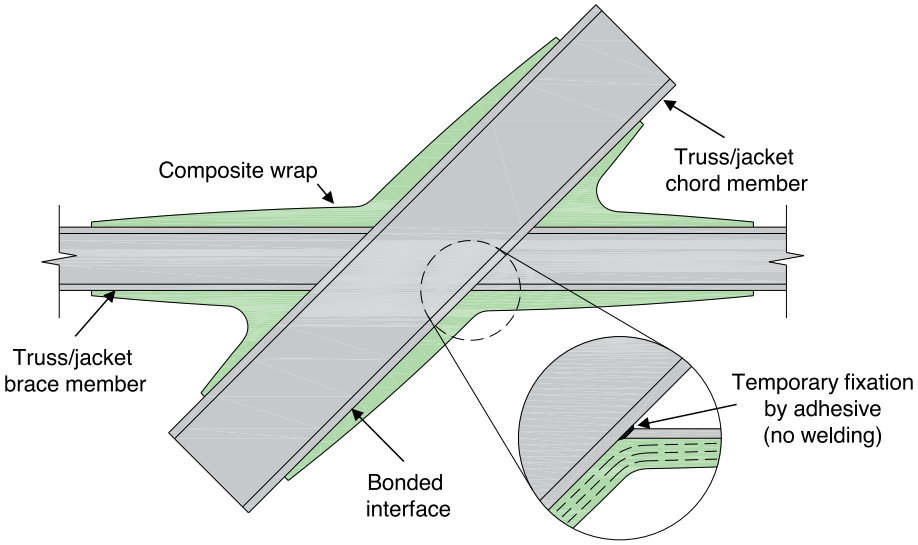

Fig. 1. Concept of wrapped composite joint.

debonding or crack length. However, strain gauges can only measure strain distribution along single lines, which cannot be used for full field measurements. Another disadvantage of utilization of strain gauges is that sticking them on the surface or within layers of the composites may lead to unnecessary damage to the material. During recent years, the non-destructive technique (NDT) has been widely used for mechanical damage assessment in composite structures [13,14], especially for monitoring the debonding at composite-to-steel/concrete interface. Current NDT techniques developed for civil engineering application include the use of: Acoustic emission (AE) [15,16], ultrasonic guided waves [17–19], infrared thermography [20,21], X-ray radiography [22], and digital image correlation (DIC) [23,24] et cl.

Among these NDT techniques, the DIC technique has been widely used for monitoring debonding between composite and steel/concrete/masonry substrates due to its advantages of non-contact, full field and real-time measurements. DIC employs tracking and image registration techniques for accurate 2D and 3D measurements of deformations and strains on surfaces of specimens. For example, Bahman Ghiassi [25], Pei Zhang [26] and Mohamad Ali-Ahmad [27] investigated debonding between FRP and substrates under quasi-static monotonic loads by DIC. Strain contours were captured under different load levels, where increased strains indicated crack initiation or debonding at the interface. In their studies, a formula was proposed to approximate strain distribution along the bond length, such that the fully debonded zone, stress transfer zone (effective bond length) and bonded zone can be depicted quantitatively. The DIC method was also applied for investigating debonding behaviour under fatigue loading [28]. The strain plateau along the CFRP plate represented the debonding length, which increased gradually with the increasing number of loading cycles. Other researchers [29] also employed gradient of surface strain to quantify debonded areas: a contour of high strain gradient indicates the debonding front and the region bounded by this contour, with negligible strain gradient, is the debonded area. Artificial delamination/debonding at the interface was used in **Ref.** [30,31] in order to validate the crack monitoring method based on surface strain from DIC. The results showed that the location of the artificial delamination can be effectively detected by DIC strain contours. The DIC results were also comparable with results from finite element (FE) models. It is worth noting that the thickness of the material above the delaminated interface may have influence on the monitoring results. It can be seen from previous studies

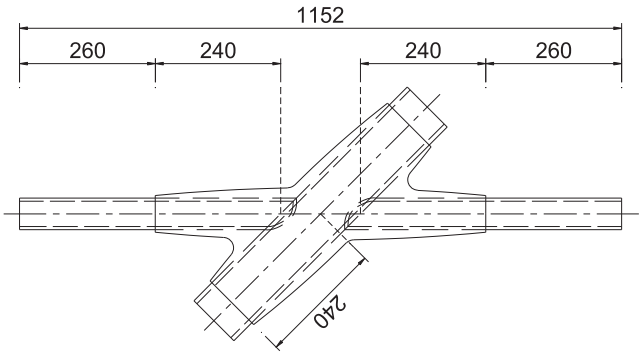

Fig. 2. Geometry and dimensions of X-45 wrapped composite joint.

[25–31] that DIC as a NDT method can be effectively used to monitor debonding at the composite/substrate interface. However, most of the debonded/delaminated interfaces monitored in the existing research are beneath a very thin laminate with constant thickness. Monitoring technique for debonding with complex geometry (i.e. under thick laminates with variable thickness) needs to be further developed, and the finite element method provides new possibilities.

Due to development of finite element (FE) software and computer science, numerical analysis has been widely used to investigate FRP-strengthened structures during the past decades. For simulating debonding or delamination behaviour at the interface via FEA, the most commonly used technique is the cohesive zone model (CZM) [32,33], which assumes a traction-separation law to simulate crack initiation and propagation. Another LEFM-based method is the Virtual Crack Closure Technique (VCCT) [32], which is widely used for calculating strain energy release rate (SERR) at crack tips. A lot of work has been done till now to simulate debonding/delamination behaviour of bonded interface with simple geometry by 2D or 3D finite element models based on VCCT [34–36], where not only the SERR but also the crack shape (for 3D models) can be captured. In combination of direct cyclic analysis [37], VCCT can be employed to simulate crack growth and extract SERR development under fatigue loading [34,38]. Instead of modelling fatigue test directly, Yiding Liu et cl. [39] used a simple but efficient way to capture SERR development during fatigue loading by running several static models with different predefined crack lengths.

In this paper, a novel technique for monitoring debonding at the composite-to-steel interface is proposed and implemented for in-depth interpretation of failure modes of wrapped composite joints under fatigue tests. 3D Digital Image Correlate (DIC) system is employed for monitoring displacement and strain distribution of the specimens. A detailed 3D finite element model of such joint is built in ABAQUS and validated against static testing results in terms of initial stiffness and surface strain distribution. The novel monitoring technique of debonding at the composite-to-steel interface is proposed based on surface strain variation, captured by DIC, and the strain threshold for determining debonding crack lengths are obtained from FE model with embedded cracks on the chord and braces. The FE model is also employed to measure strain energy release rates at the interface, which is used to further explain failure mechanisms of tested specimens based on fracture mechanics. The FE analysis and crack monitoring results are helpful for fatigue behaviour characterizing and fatigue life prediction of wrapped composite joints in the future.

2. Experiment description

In the experimental program, X-45 wrapped composite joints are tested under tensile fatigue loads. Geometry and dimensions of the wrapped composite joints is shown in Fig. 2. The materials, production procedure and the naming rule of these specimens are detailed in the previous research [10]. Specimens included in this paper and the corresponding load ranges are shown in Table 1. Two tensile-tensile fatigue load ranges, that is 10-110kN (low) and 15-165kN (high), with R = 0.1 are selected, which correspond to nominal stress ranges of 141 MPa and 212 MPa in the braces with steel profile of Φ 60.3 × 4, respectively. The fatigue tests are conducted by the PCX 001 Hydraulic Wedge Grip, with a dynamic loading capacity of ± 600kN. The test set-up is shown in Fig. 3. More details about test set-up and loading protocol can be found in **Ref.** [10].

3D Digital Image Correlate (DIC) system is employed for displacement measurement and strain monitoring of the specimens, which is critical for calculating stiffness degradation and determining debonding lengths afterwards. The DIC system used in current research is 3D GOM ARAMIS DIC with 12 million pixels, 12 mm lenses and polarized blue led lights, as can be seen in Fig. 3(a). Spackle pattern with white background and random black dots, needed for DIC, is applied on one side of the specimen, (see Fig. 3(b)). The other side is left unpainted for visual observation of cracks in the composite wrap. During post processing, the subset size used in this analysis is 30 pixels, while the distance between adjacent subset centers, the step size, is 15 pixels. The DIC system is used for measuring relative displacement between top/bottom and middle facet points created in GOM Correlate software as shown in Fig. 4. Note that the top and bottom facet points are around 340 mm away from the middle point, which are located on the steel braces and near the wrapping ends. In such circumstance, the stiffness degradation of segments, corresponding to the joints between the top and bottom brace members and the chord in the middle, can be calculated separately as:

$$k(N) = \frac{F_{\max}(N) - F_{\min}(N)}{\Delta L_{\max}(N) - \Delta L_{\min}(N)} \tag{1}$$

where N represents number of cycles, $F_{\max}(N)$ and $F_{\min}(N)$ are the maximum and minimum applied forces at the Nth cycle, $\Delta L_{\max}(N)$ and $\Delta L_{\min}(N)$ are the relative displacements between the facet points (elongations of the top and bottom braces) at the maximum and minimum loads, respectively. Further usage of the DIC system is to monitor strain distribution on the surface of the composite wrap. The strain concentration, crack propagation and failure modes of the specimens are observed real-time during the test, and processed afterwards in more details.

Stiffness degradations of the top/bottom braces from different specimens, calculated according to DIC results, are shown in Fig. 5. It is shown that the joint stiffness in all cases decreases steadily during the loading process due to possible accumulated damage in the composite material and debonding at the composite-to-steel interface. Under lower load range of 10-110kN, which corresponds to nominal stress range of

Table 1
Results of fatigue tests on wrapped composite joints.

Load ranges (nominal stress ranges)	Specimens	Number of cycles	Stiffness degradation (%)	
			Top brace	Bottom brace
10-110kN (141 MPa)	cX45-Ss-T_F2.1	3,419,862	19	11
	cX45-Ss-T_F2.2	3,074,671	7.6	6.6
16-165kN (212 MPa)	cX45-Ss-T_F3.1	59,739	37	54
	cX45-Ss-T_F3.2	81,207	55	32

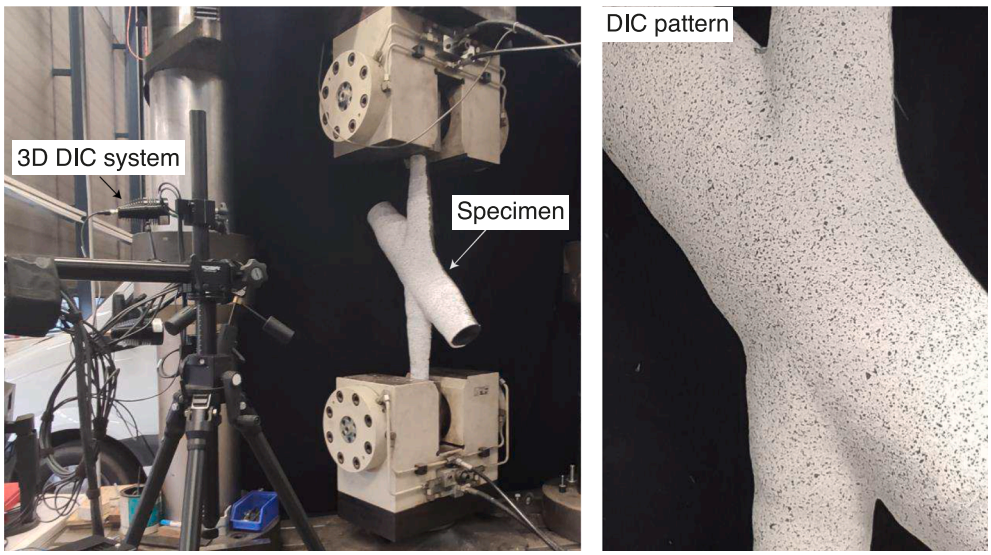

Fig. 3. Test set-up, DIC system and spackle pattern.

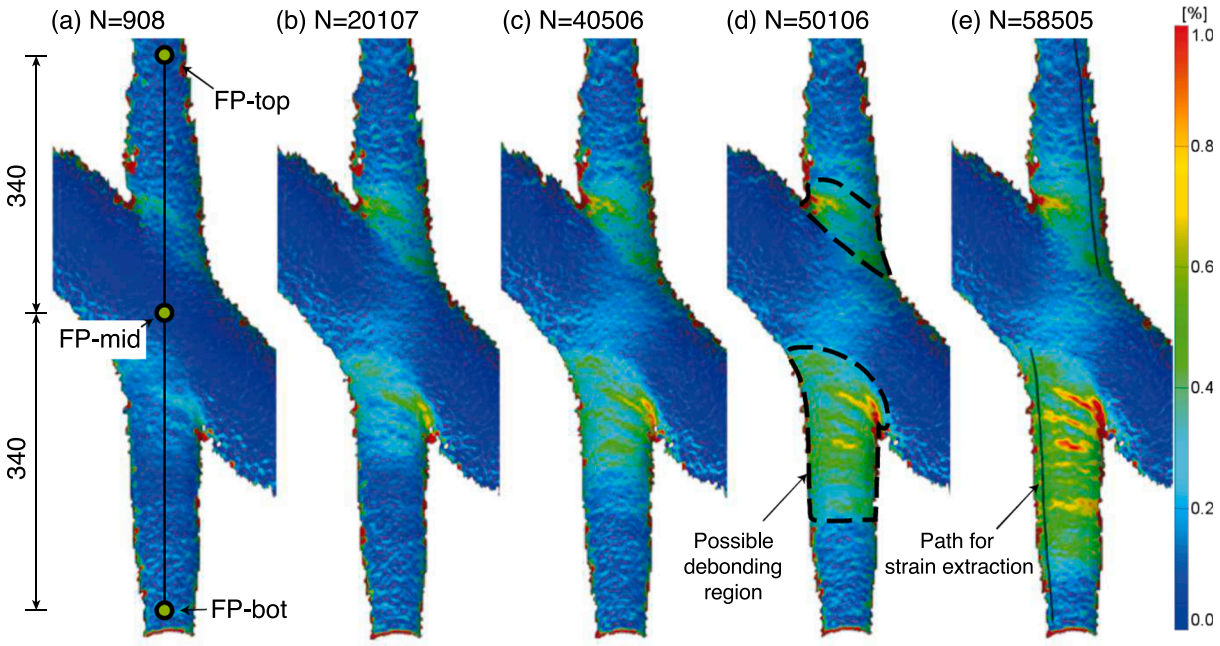

Fig. 4. DIC contour of progressive strain increase on surface of cX45-Ss-T_F3.1.

85 MPa in the brace, less than 20% of the original stiffness is lost for any of the top or bottom braces after even 3 million cycles. Under the load range of 15-165kN (nominal stress range of 212 MPa in the brace), the braces from specimen cX45-Ss-T_F3.1 show a stiffness degradation of 37–55% after 57,000 cycles. Similarly, the braces from specimen cX45-Ss-T_F3.2 exhibit a stiffness degradation of 30–55% after 80,000 cycles. More details of stiffness degradation related to different braces are summarized in Table 1. It should be noted that the stiffness degradation used to control and to stop the cyclic loading is the global stiffness of the whole joint, namely the average value of stiffness degradation of the top and bottom braces. However, it is shown from Fig. 5 that one brace always degrades more while the other one degrades less. This can be also reflected by Fig. 4, which shows typical DIC contour plots of major principal strain on surface of specimen cX45-Ss-T_F3.1 at the maximum loads at different numbers of cycles. It shows that the localized high strains only exist in the root of braces which further propagate towards the end of the composite wrap. Development of strains on top and bottom braces are quite different, indicating larger crack propagation and stiffness degradation rates at the bottom side. The increase of major principal strains in certain regions on the surface of composite wrapping (light blue and green areas) can indicate both the composite-to-steel debonding failure, as well as the smeared material damage and delamination within the composite wrap. The governing failure mode is debonding of the interface between composite wrapping and steel profiles induced by stress concentration. This is confirmed by post-test cutting of the specimens in **Ref.** [10]. Therefore the strain increase registered by DIC is mainly due to debonding at the interface. The different behaviour between the top and bottom brace within the same specimen may result from different roughness of the surface of steel profiles, which has been confirmed by previous study [10].

Strain distribution along surface curve defined on the brace as shown in Fig. 4 is further extracted for determining the debonding length. One

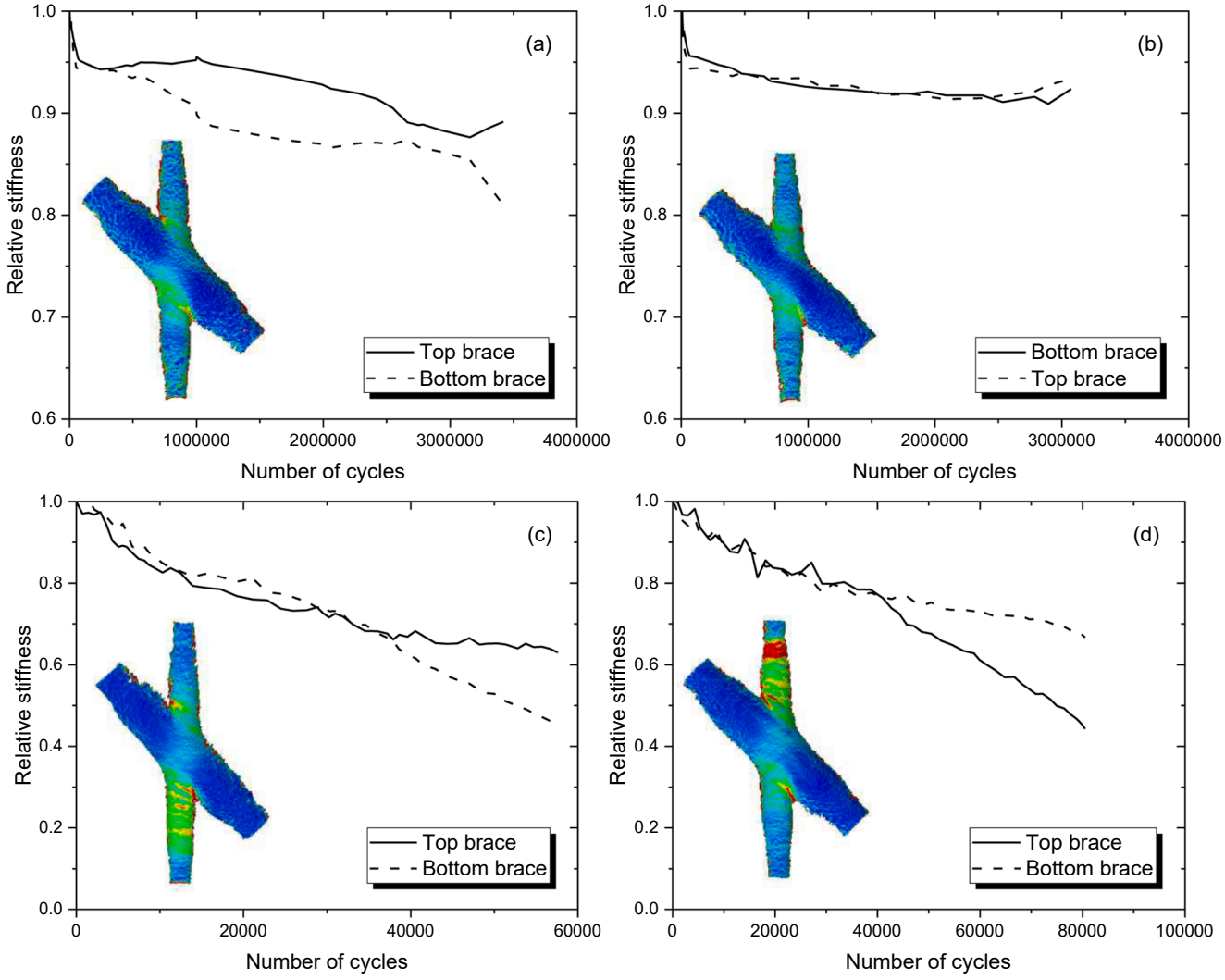

Fig. 5. Decoupled stiffness degradation of top and bottom braces (a) cX45-Ss-T_F2.1; (b) cX45-Ss-T_F2.2; (c) cX45-Ss-T_F3.1; (d) cX45-Ss-T_F3.2.

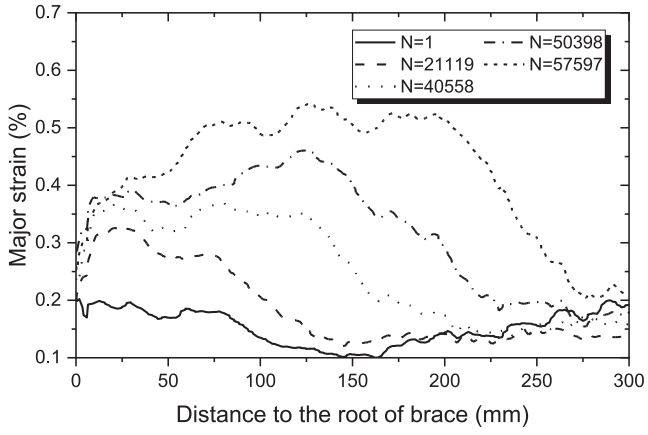

Fig. 6. Strain distribution along bottom brace of cX45-Ss-T_F3.1.

example of extracted strains along the bottom brace of cX45-Ss-T_F3.1 at different number of cycles is shown in Fig. 6. In order to remove scatter resulting from DIC measurements, all these curves are smoothened with adjacent-averaging method during post-processing of data using ORIGIN software. It shows that at initial stage, the surface strains mainly develop around root of the brace, followed by gradual decrease and again slight

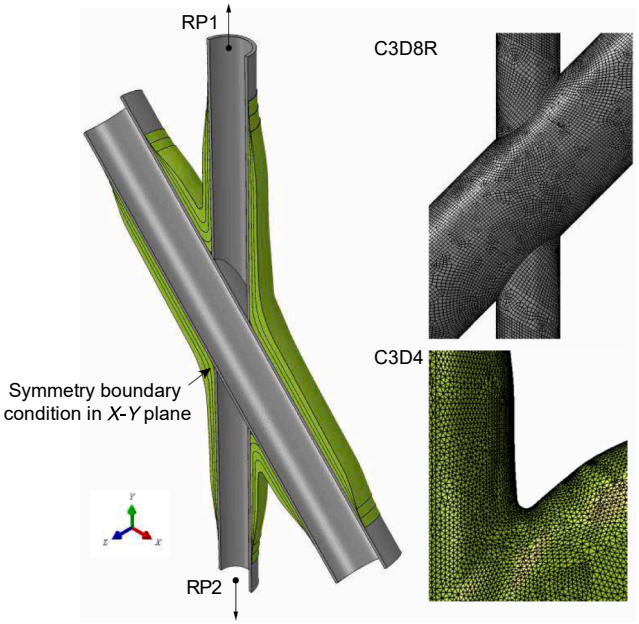

Fig. 7. Finite element model and mesh strategy of wrapped composite joints.

Table 2
Material properties of GFRP composites.

Material name	Elastic constants (GPa)	Poisson's ratio
Composite wrap (GFRP)	$E_1 = E_2 = 12.0$, $E_3 = 6.6$, $G_{12} = 3.1$, $G_{13} = G_{23} = 2.5$	$\upsilon_{12} = 0.15$, $\upsilon_{13} = \upsilon_{23} = 0.3$
Steel members (S355)	$E_1 = 210$	$\upsilon = 0.3$

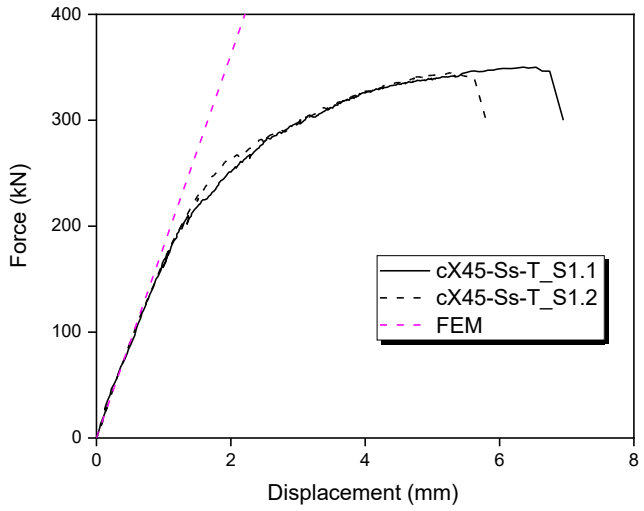

Fig. 8. Load displacement curves (source of test data: [9]).

increase towards the end of composite wrap. With the increase of loading cycles, the peak strain increases and develops gradually towards end of the wrap, indicating debonding propagation at the composite-to-steel interface. It should be noted that the surface strain distribution will also be influenced by at least another two phenomena. One phenomenon is the nonlinear in-plane and through thickness shear behaviour of the thick composite laminate with complex (variable) geometry. Another phenomenon is the interaction with the chord debonding. The debonding on the chord interface is contributing deviation of the strain filed on surface of braces and vice versa. To overcome the influence of these multiple factors, an innovative combined DIC and FEA method is proposed to capture crack development along the brace and chord quantitatively in next sections. FE model is built to provide insight into supposed strain distribution resulting from the complex geometry and stiffness transitions due to non-uniform thickness of composite and possible developed debonding crack.

3. Finite element modelling

3.1. Modelling strategy

To further reveal failure mechanisms and assist crack propagation monitoring at the steel-to-composite interface, a detailed finite element model is built in Abaqus software package [37]. The geometry of steel tubes follows the designed drawings of the specimen, while the dimensions of composite part (thicknesses on flat parts and corners) are determined with the help of 3D scanning of the specimen. The composite parts are modelled with 3 layers as has been applied during the production process. More details about the production of specimens and joint geometry were given in [9] and [10]. Due to the symmetric geometry, only half of the joint is modelled to reduce the computation time, as shown in Fig. 7. Surfaces representing the end cross sections of the braces are coupled to reference points, RP1 and RP2, as shown in the figure. All degrees of freedom except for the U2 (y) direction are constrained for the reference points to replicate the fixation constraints at the tube ends due to clamping in physical test. The load is applied by vertical displacement on both RP1 and RP2. Symmetric boundary conditions were applied in the middle (cut) plane.

Linear, hexahedral solid elements, C3D8R, with reduced integration are used for the brace and chord steel members. Linear tetrahedron elements, C3D4, are used for the composite wrap due to its complex geometry. The composite parts are modelled as 3 non-uniformly thick laminates by 3D solid instead of multiple plies by shell elements since the delamination is insignificant during the fatigue tests, as shown in cut specimens in **Ref.** [10]. Mesh size of all the elements is chosen as 2.83 mm after the sensitivity study. At least 4 elements through the thickness of the steel tubes are included to accurately model possible local bending behaviour.

Material of composite wrap is considered as transversely isotropic. The elastic constants can be found in Table 2, which are obtained through standard material tests on the GFRP laminate (E_1, G_{12} and ν_{12}), as shown in [9] or based on classical laminate theory and rules of mixture for data not obtained directly by tests. For the steel parts, isotropic elastic properties (E = 210GPa and ν = 0.3) are defined. Plasticity, ductile damage and shear damage are not considered. The GFRP thick laminate of the composite wrap and steel components remain in elastic stage under the maximum fatigue load of 165kN as discussed in Section 3.2.

In order to calculate the strain energy release rates (SERRs) at the debonding crack tips of the composite-to-steel interface, the bond behaviour between steel members and composite wrap is simulated by VCCT [37]. As the calculated SERR is sensitive to mesh size at the crack tip, a mesh convergence study is carried out before formal analysis to obtain accurate results. A size of 2.83 mm as shown in Fig. 7 is found to be appropriate for both composite and steel part considering computing accuracy and efficiency. Although in this study, crack propagation under static load will not be considered, the mixed mode behaviour and fracture criterion is still defined with Benzeggagh–Kenane Law [37]:

$$G_{eqc} = G_{Ic} + (G_{IIc} - G_{Ic})\left(\frac{G_{II} + G_{III}}{G_T}\right)^{\eta} \quad (2)$$

where G_{eqc} is the critical SERR, G_{Ic} and G_{IIc} are critical mode I and mode II SERR, $G_T = G_I + G_{II} + G_{III}$, and $\eta = 1.8$. Relatively high values of G_{Ic}, $G_{IIc} = G_{IIIc}$, i.e. 100 N/mm, are used here to guarantee that the fracture criterion of $G_T \geq G_{eqc}$ will not be met under the applied load. Under such circumstance, crack propagation will not happen so that SERR at predefined crack tips can be calculated.

3.2. Modelling results and validation

The initial joint stiffness obtained from FEA using anisotropic elastic material for GFRP, (see Fig. 8**),** is 184 kN/mm, while the average value from test results is 172.15 kN/mm according to [9], which is within 6.5% accuracy. The model is considered to be satisfactory for elastic analysis to calculate surface strain distributions, as well as the strain energy release rates at the crack tip. Those are obtained for the initial (undamaged) state and the following analysis where debonding cracks at the interface are embedded to simulate damage due to the load cycles. It should be noted that near the maximum load of 165kN in fatigue load cycles, the stiffness of load–displacement curves of the ultimate load tests show slight degradation (up to 5%) as shown in Fig. 8. This is attributed to onset of non-linear behaviour of the composite wrap through the thickness in the ultimate load tests with the monotonic load. Such stiffness deviation may have influence on strain distribution on the surface of composite wrap at the analysed load level of 165kN when utilizing the surface strain distribution as starting point for monitoring debonding at the interface. Potential influence of slight non-linear behaviour of the composite wrap on debonding crack length estimation by the proposed combined DIC-FEA method is assessed and discussed by creating another no-linear FE model. In the non-linear model,

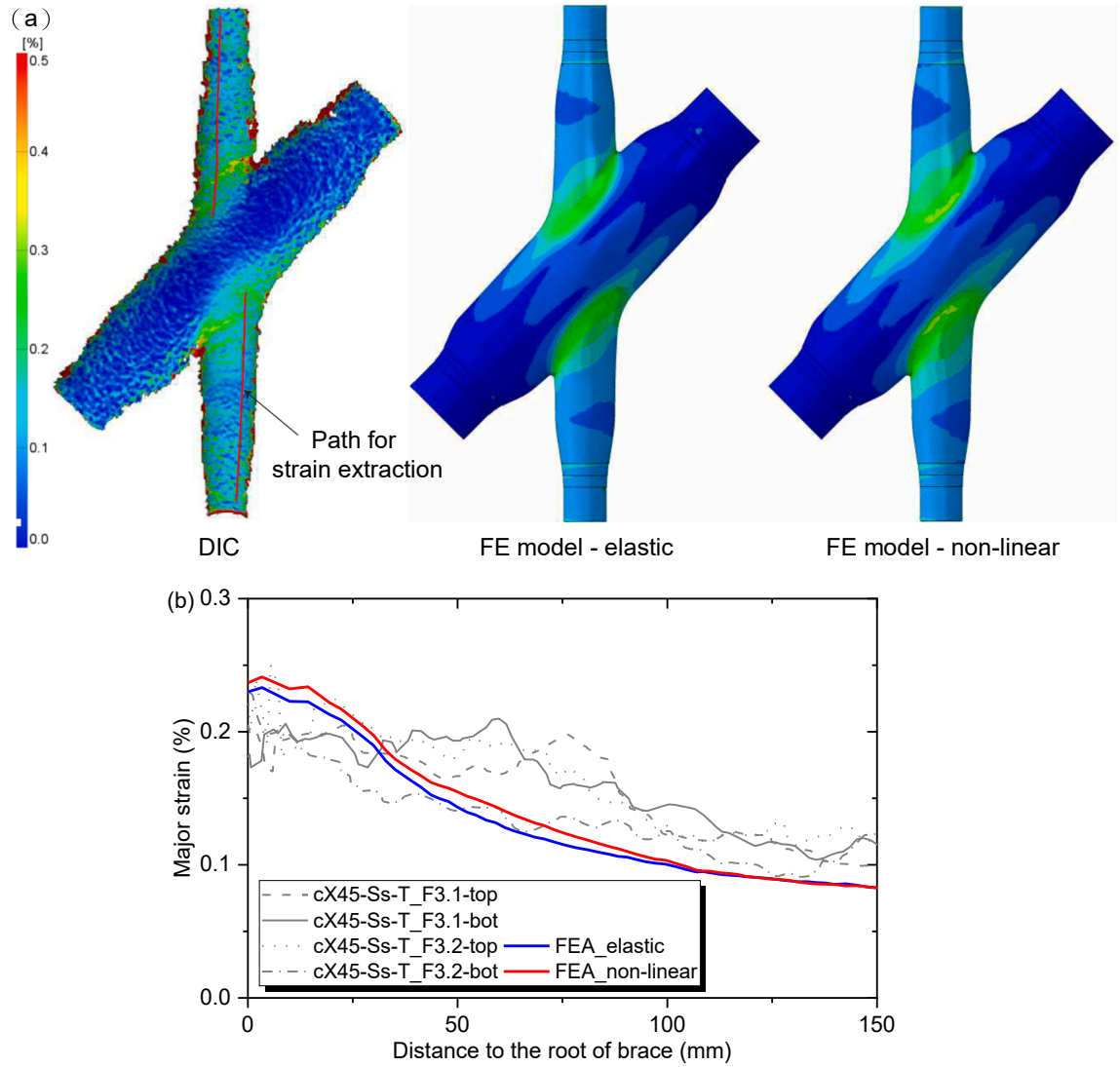

Fig. 9. Major principal strain distribution comparison between DIC and FEA (at 165kN load, $N = 0$, $l_b = l_c = 0$ mm): (a) Contour of strain distribution on surface of specimen (b) Strain distribution along defined path.

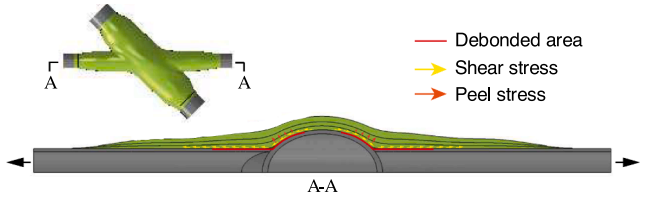

Fig. 10. Debonding mechanism on both composite-to-brace and chord interface.

Hill's plasticity is used to simulate non-linear through-thickness behaviour of the composite wrap. Through-thickness shear stress is limited to 30 MPa which corresponds approximately to inter-laminar shear strength.

Further comparison of surface strain distribution from DIC and FEA results is conducted herein. Fig. 9(a) shows the contour plots of major strain distribution on the surface of the specimen from DIC measurement and FEA results. Analyses with and without non-linear through thickness behaviour of the composite wrap material under 165kN are shown. The pattern of major principal strain distribution from DIC resembles well those from both FEA results. The strain is concentrated at the brace-to-chord corners and decreases gradually towards the end of brace. A path is defined along the brace as shown in Fig. 9(a), from which major principal strain is extracted from DIC and both FEA results for further comparison. As shown in Fig. 9(b), the strain distribution along the brace from DIC measurement matches well with FEA results, although there are a lot of noises because of relatively low level of strains (0.3%) that are measured. Results from both FEA methods are also in agreement with each other, which means that the influence of material plasticity and damage is insignificant on strain distribution on the surface of the model. To increase the computing efficiency, all the models in this paper will be run without any definition of plasticity and damage in the materials considering its negligible influence.

4. Debonding crack propagation analysis

4.1. Method of debonding crack propagation monitoring using combined DIC and FEA data

For all the experiments analysed here, the dominate failure mode under fatigue loading is debonding at the composite-to-steel interface. More details about the test results were given in [10]. Debonding cracks are propagating at the composite-to-brace interface due to shear stress, and at the composite-to-chord interface due to both shear and peel

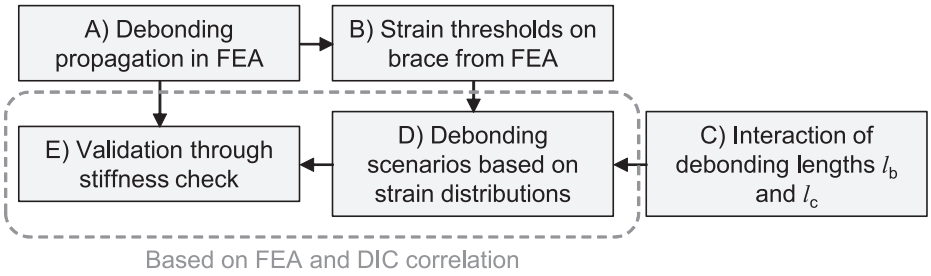

Fig. 11. Steps for determining crack length on the braces and chord.

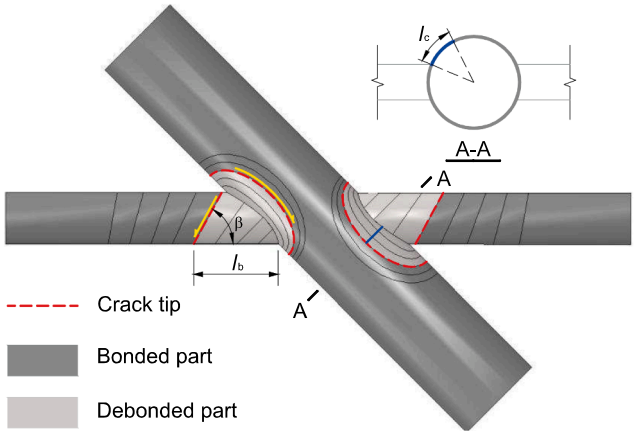

Fig. 12. FE model with different pre-cracks on the brace and chord.

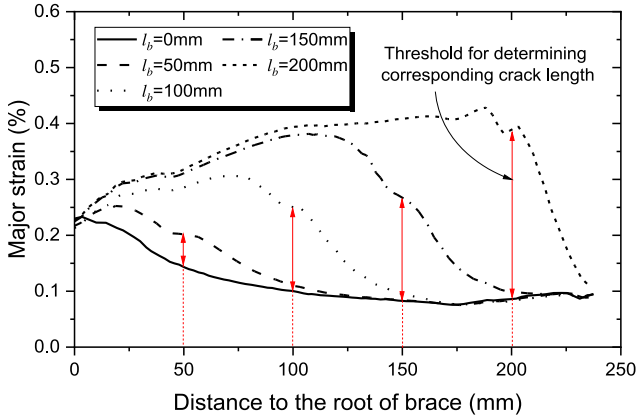

Fig. 13. Strain distribution extracted from FE model with different precracks l_b on the brace (l_c = 0 mm).

stresses as shown in Fig. 10. Understanding and quantifying the crack propagation process during the test is of great importance for development of prediction methods for fatigue behaviour of the wrapped composite joints. As mentioned above, monitoring the debonding of the joints with complex geometry by using the strain distribution on the surface of composite wrap still remains a problem, especially when interaction between debonding on two different parts, i.e. chord and brace, exists. In the previous study [10], a constant threshold of difference between strain distribution curves from the first and *N*th cycle was used as the cut-off point to determine the debonding length, while the interaction between debonding on the chord and brace was not considered. In this paper, an innovative monitoring method with combination of DIC results and FEA analysis is proposed. The strain thresholds for different debonding lengths are determined by FE models with artificial embedded cracks. The steps are listed as in Fig. 11.

Brief explanation of step A to E is given as follows:

Step A) Analysis of FE models with a number of artificial debonding cracks of different lengths on the braces and chord;

Step B) Determining of surface strain variation thresholds in function of crack lengths on the braces and the chord based on the FEA data;

Step C) Parametrizing the interaction between the crack length on the braces and on the chord;

Step D) Calculating crack length on the brace in function of number of cycles from DIC using strain variation thresholds obtained from FEA. Multiple sets of data are generated assuming a range of interaction parameter from Step C;

Step E) Finding the best fit interaction parameter by comparison of stiffness degradation curves from DIC and FEA.

Among these steps, step A provides strain thresholds for step B and stiffness vs. crack length relationship for step E. After obtaining strain thresholds through step B and defining interaction between cracks on the braces and chord by step C, different debonding scenarios on the braces and chord can be obtained in step D. The steps D and E can metaphorically be represented as equivalent to solving algebraic system with 2 unknowns with 2 independent equations. The "unknowns" are 1) the interaction function of cracks on the braces and chord, and 2) the crack length on the brace. The "equations" are the 1) stiffness degradation curve from DIC (test) infunction of interaction and crack length on the brace and 2) stiffness degradation curve from FEA in function of interaction and crack length on the brace. The steps A to E are further described in more details substantiated by results from X45 joints subject to cyclic loading at two load levels:

Step A) FE models with pre-cracks of different lengths on the braces and chord are created and the load is applied corresponding to the maximum load in the cyclic tests, which are 110 kN and 165 kN in this study. The crack patterns are assumed to follow the shapes obtained in a FE model analysing crack propagation, by help of cohesive load modelling, in static ultimate load test (not shown in this study). As shown in Fig. 12, cracks on the brace start as a triangle from the obtuse corner. The crack length on the brace, l_b, is defined as the length of one side of that triangle near the obtuse corner. The angle between the crack tip and the brace edge β will increase as the crack propagates converging towards a crack perpendicular to the brace axis. Cracks on the chord are defined as several semicircles expanding from the chord-brace intersection root. The length of the arc staring from the saddle point to the mid-point of the crack tip is defined as the crack length l_c on the chord. The crack length on the brace increases in the FE models from 0 mm to 200 mm in steps of 25 mm, while the crack length on the chord starts from 9.5 mm and increases to the middle of the chord in steps of 10 mm. For the maximum possible crack length on the brace, 200 mm is chosen since it is near the wrapping ends, above which the SERRs may exceed the critical value. For cracks on the chord, it is assumed that the crack from one side will not extend to the other side since tensile load from one side will not cause shear and peel stresses at the interface of the chord on the other side. Considering different combinations of crack lengths on the brace (l_b) and on the chord (l_c), a total number of 45 models are analysed. In the FE model, interaction property for the cracked part is defined with hard contact for the normal behaviour and frictionless for

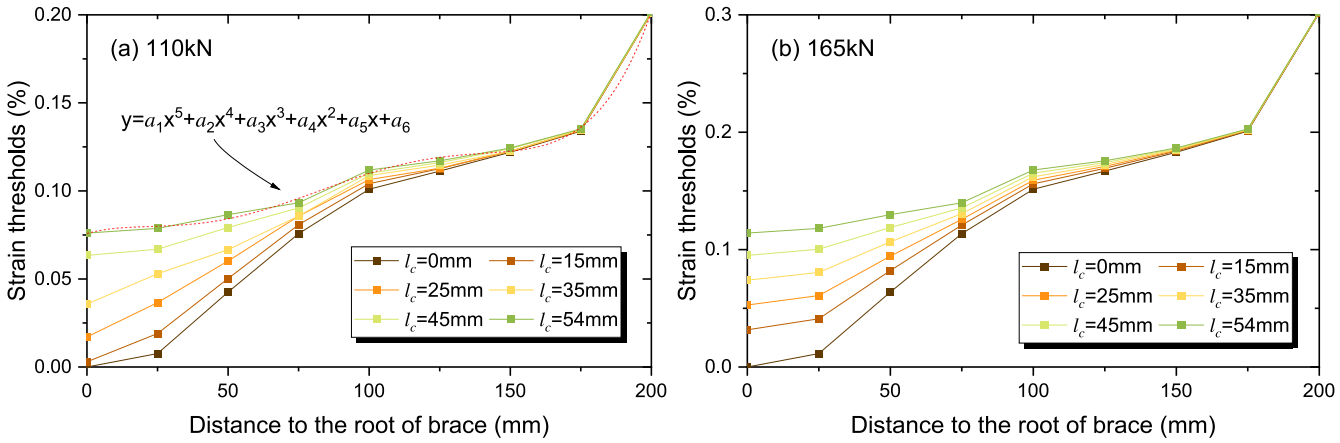

Fig. 14. Strain thresholds in function of crack length on the brace and chord (a) 110kN without considering interaction between debonding on the chord and brace; (b) 165kN without considering the interaction.

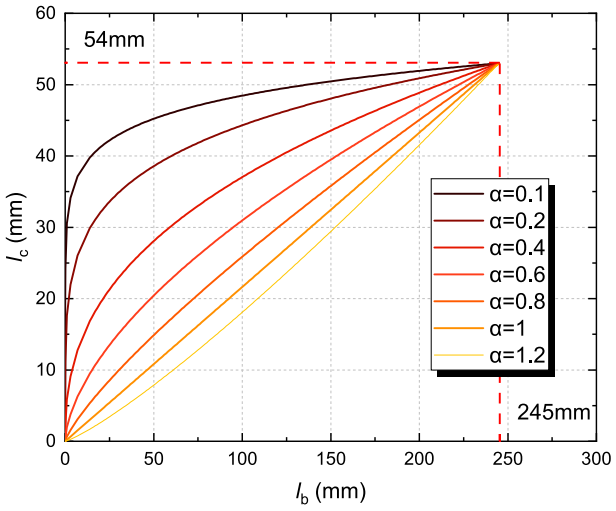

Fig. 15. Relationship between l_c and l_b with different α values.

the tangential behaviour. For the bonded part, the bonding behaviour is modelled by VCCT to obtained the strain energy release rates (SERR) in at the crack fronts.

Step B) For each FE model, strain distributions along the predefined path as shown in Fig. 4 are extracted at force levels corresponding to maximum loads applied in the fatigue tests. The difference of strain curves at the crack tip between FE model with *l*mm artificial crack and the initial FE model without the crack (0 mm) is the threshold for determining the corresponding crack length in the DIC results. Without the interaction between brace and chord being considered, strain distributions from model with $l_c = 0$ mm crack on the chord and different crack lengths l_b on the brace are shown in Fig. 13. The threshold will increase nonlinearly with respect to the increase of the crack length. This is because the thickness of the composite wrap decreases towards the wrap end. The relationship between strain thresholds and different

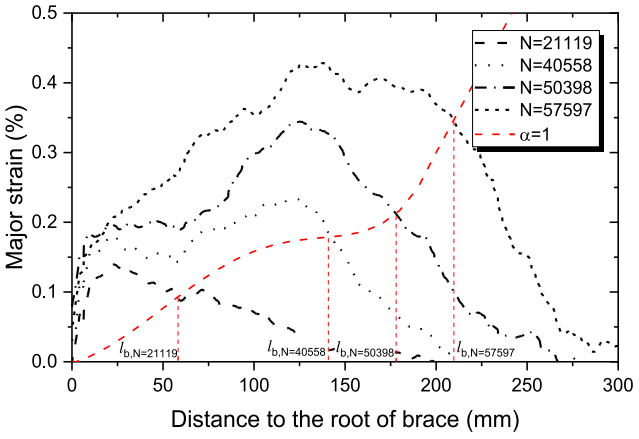

Fig. 17. Method of determining crack lengths on the brace.

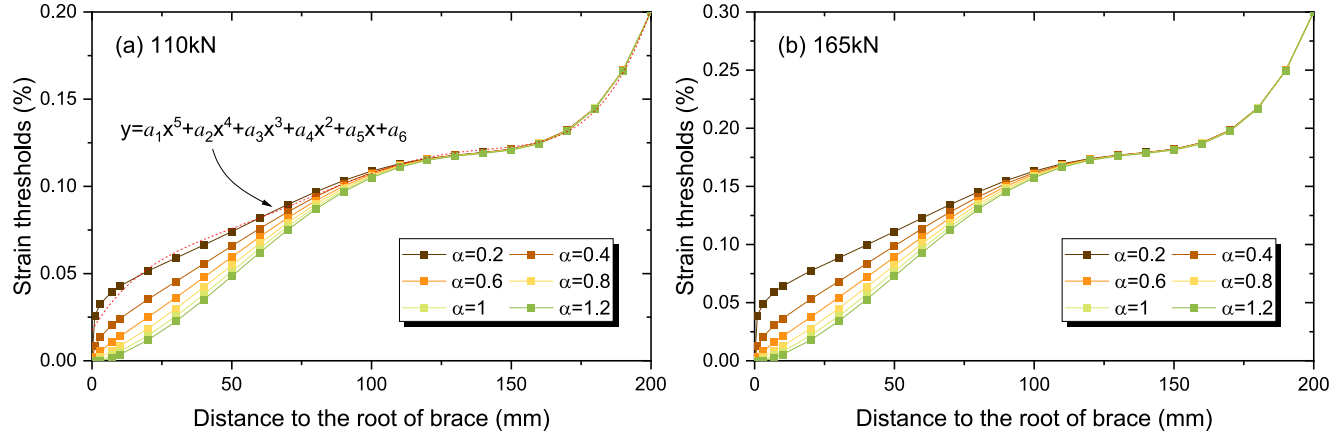

Fig. 16. Strain thresholds in function of crack length on the brace and chord (a) 110kN with considering the interaction; (b) 165kN with considering the interaction.

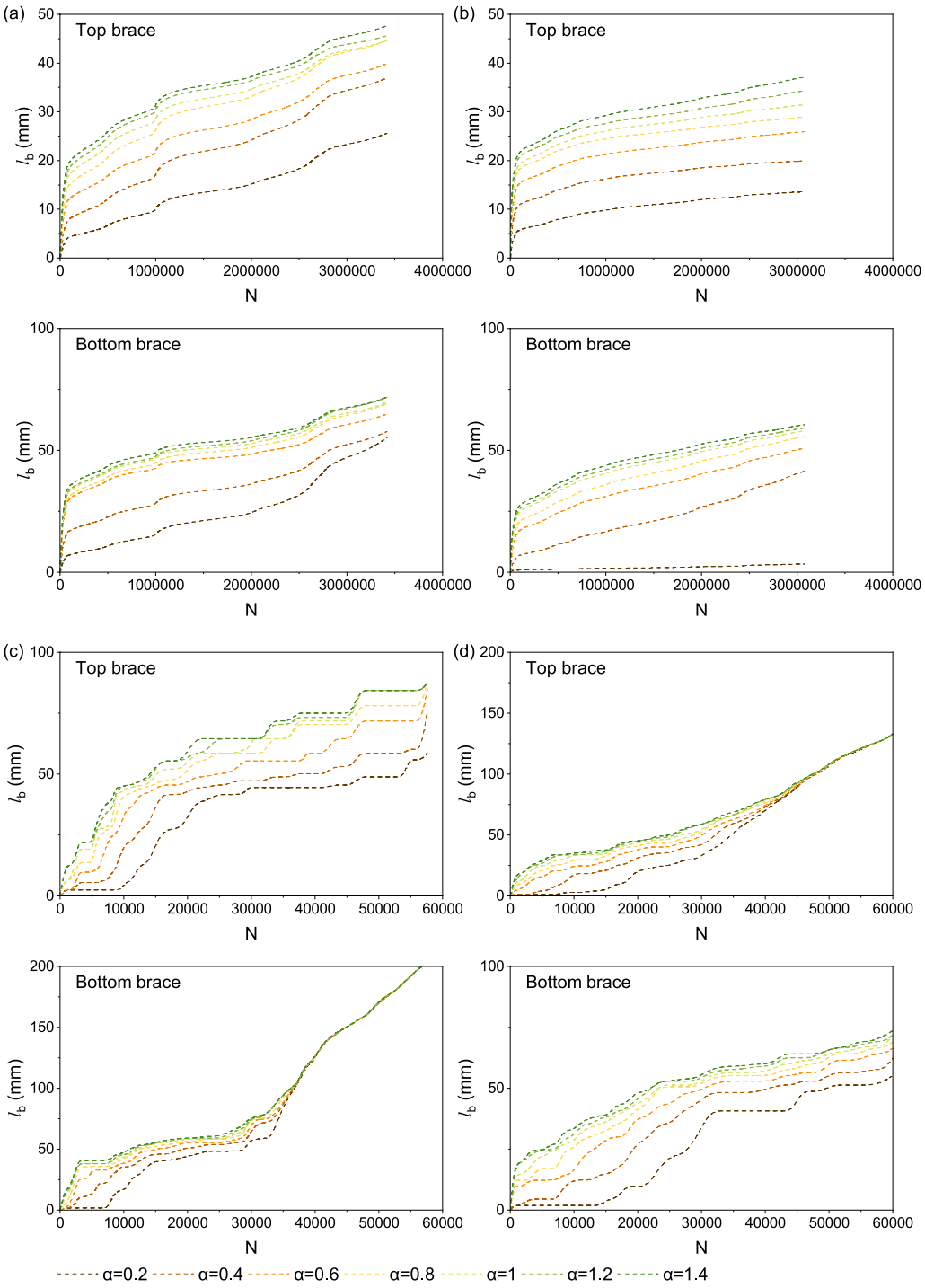

Fig. 18. Calculated crack lengths on the brace with different α values (a) cX45-Ss-T_F2.1; (b) cX45-Ss-T_F2.2; (c) cX45-Ss-T_F3.1; (d) cX45-Ss-T_F3.2.

crack lengths on the brace under two load levels used in this study, 110 kN and 165 kN, is shown in Fig. 14**(a)** and **(b)**. The influence of debonding on the chord is also taken into account by repeating the FE analysis with different values of l_c. The results show that crack propagation on the chord will lead to increasing strain thresholds for determining the crack length on the brace near the root, while above $l_b = 100$ mm the influence will be insignificant. This means that without considering debonding on the chord, the crack propagation rate on the brace in the initial region, up to $l_b = 100$ mm in this study, will be overestimated.

Step C) As crack on the brace propagates, crack on the chord will also develop. The FE model used for ultimate load analysis (not shown here) indicates that debonding will first develop at the chord interface followed by domination of debonding on the brace. Confirmation of such order of debonding in cyclic load test ananlysed here is provided through strain energy release rate analysis in Section 5. Determining the crack length on the chord is not as straightforward as that on the brace. In order to overcome such shortcoming the interaction between the chord and the brace debonding is approached phenomenologically. A relationship between crack length on the chord and brace is assumed. A relationship is proposed in a form of a power law as follows:

$$l_c = l_{c.max} \times (l_b / l_{b.max})^{\alpha} \tag{3}$$

where l_c is the crack length on the chord, l_b is crack length on the

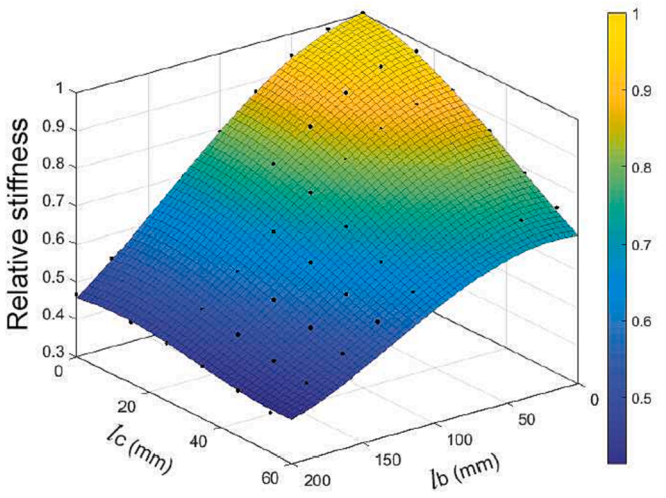

Fig. 19. Stiffness variation with different crack lengths on the brace and chord.

brace. $l_{c,max}$ is the maximum possible crack length on the chord (53 mm in this study). The maximum possible crack length on the brace $l_{b,max}$ is the distance from the obtuse corner to the end of wrap (full debonding), 245 mm in this study. α is the parameter to define different relationships of l_c and l_b while α less than 1 is adopted here to reflect that debonding on the chord is dominate at the initial stage as shown in Fig. 15. A less-likely possibility that debonding on the brace is dominant in the beginning is also considered by one value of interaction factor α = 1.2. According to the relationship defined with different α values, the strain thresholds are shown against crack length on the brace in Fig. 16(a) and (b). These threshold curves are then fitted with polynomial functions, which are convenient for calculating crack lengths on the brace from DIC data in MATLAB code. One example of the fitted formula is shown in Fig. 16(a).

Step D) Once the threshold curves in function of interaction parameter α are determined, the crack length on the brace can be obtained by calculating the X coordinates of intersection points between strain threshold curves and strain deviation curves from DIC. The strain deviation curves are obtained by subtracting DIC strain values from the first cycle on the longitudinal path from the *N*th cycles. One example of just couple of strain deviation curves at different number of cycles on bottom brace obtained from DIC data of cX45-Ss-T_F3.1 and strain threshold curve with α = 1 is shown in Fig. 17. Calculation of intersections of the strain threshold and strain deviation curves at each load cycle and for each specimen is scripted in MATLAB [40]. The calculated results for different α values are shown in Fig. 18 for top and bottom brace of all specimens. The influence of α values on calculated crack lengths is more significant for the crack lengths below 100 mm because debonding on the chord has more influence on strain distribution on the brace surface near the root. A higher α correspond to higher strain threshold such that smaller crack length will be obtained. Above 100 mm, there is no difference of calculated crack lengths for different α values.

Step E) The last step is to find the best α values, namely to unravel which interaction of the crack on the chord and the brace is most realistically represented in experiment data. This can be done by comparing joint stiffness degradation vs. crack length curves from FE analysis and test results. By extracting the initial stiffness of FE models with different crack lengths, relative stiffness of specimen can be plotted as a function of crack length on the brace and chord as shown in Fig. 19. The obtained dataset is fitted with third order polynomial in function of l_b and l_c with formula shown in **Eq.** (4). By combining Fig. 5 and Fig. 18, the relationship between relative stiffness and crack length on the brace from test results is obtained and shown in Fig. 20(a). With different α values, the relationship between stiffness and crack length on the brace from FEA is obtained and shown in Fig. 20(b). Relative stiffness obtained from test results (DIC + FEA) are plotted against relative stiffness obtained purely from FE analysis. Correlation between the two results is analysed to determine the fitness. The best α value should correspond to the highest coefficient of determination R^2. R^2 is defined by **Eq.** (5), where y_k represents test results, $\hat{y}_k$ represents predicted results and $\bar{y}_k$ is the mean value of the test results.

$$k(l_c, l_b) = 1 + a_1 l_c + a_2 l_b + a_3 l_c^2 + a_4 l_b l_c + a_5 l_b^2 + a_6 l_c^3 + a_7 l_c^2 l_b + a_8 l_c l_b^2 + a_9 l_b^3 \tag{4}$$

$$\begin{aligned} a_1 &= -8.9 \times 10^{-4}, \\ a_2 &= -4.7 \times 10^{-4}, \\ a_3 &= -1.4 \times 10^{-4}, \\ a_4 &= 1.2 \times 10^{-5}, \\ a_5 &= -2.3 \times 10^{-5}, \\ a_6 &= 1.1 \times 10^{-6}, \\ a_7 &= 1.3 \times 10^{-7}, \\ a_8 &= 1.6 \times 10^{-8}, \\ a_9 &= 5.5 \times 10^{-7}; \\ R^2 &= 0.99 \end{aligned}$$

$$R^2 = 1 - \frac{\sum_{k=1}^{n_t} (\hat{y}_k - y_k)^2}{\sum_{k=1}^{n_t} (\hat{y}_k - \bar{y}_k)^2} \tag{5}$$

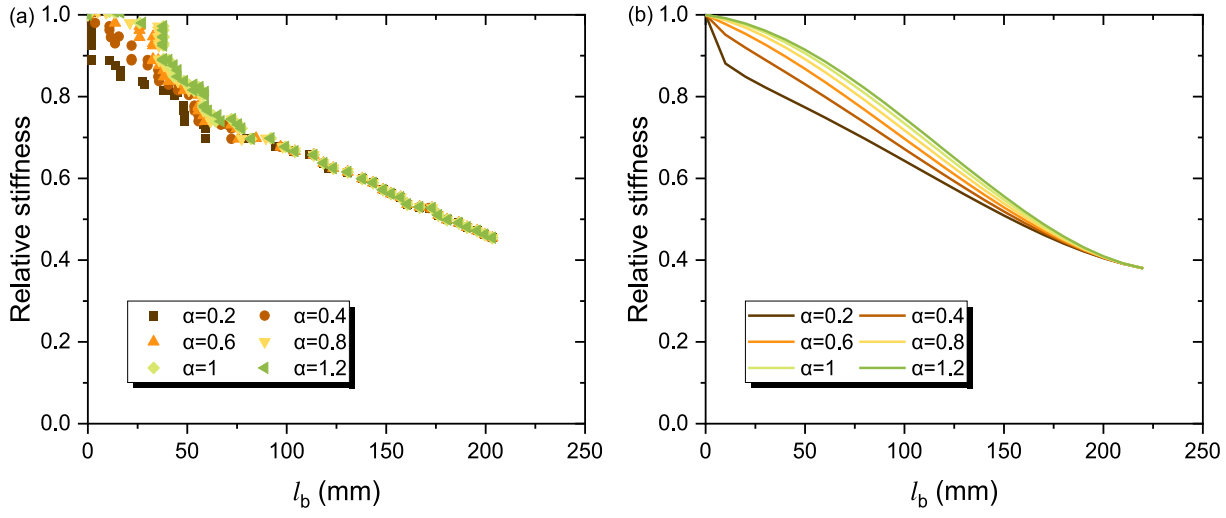

Fig. 20. Relationship between relative stiffness vs. crack length on the brace (a) test results (b) FE results.

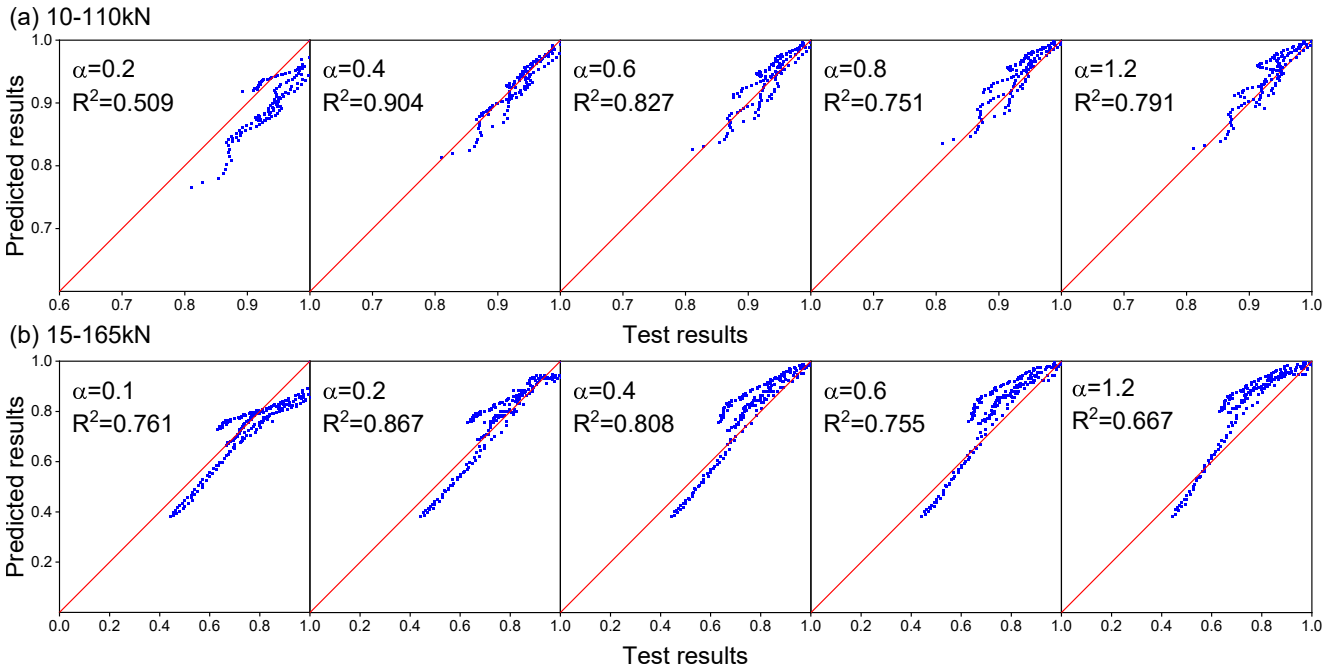

Fig. 21. Correlation analysis between stiffness obtained from test and FEA with different α values (a) specimens under 10-110kN (b) specimens under 15-165kN.

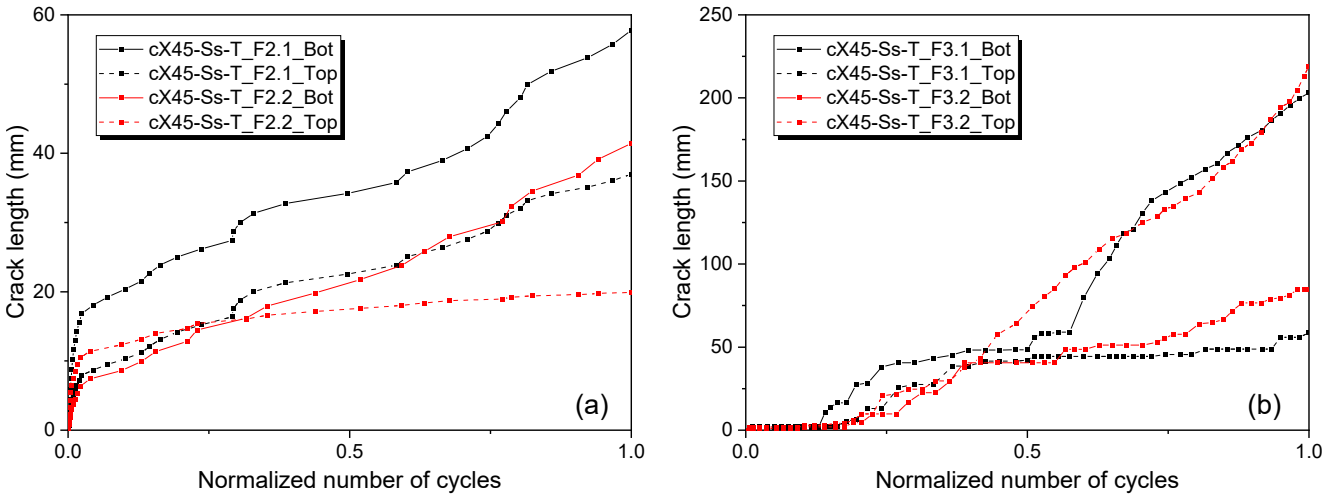

Fig. 22. Crack length on the braces obtained by the newly proposed method for different specimens (a) specimens under 10-110kN (b) specimens under 15-165kN.

4.2. Results of crack propagation analysis on wrapped composite joints

Results of correlation analysis described in Step E are shown in Fig. 21. It can be seen that under both lower and higher load range, stiffness obtained from test and FEA shows quiet good correlation for all the α values below 1.The best fit αα values are 0.4 and 0.2, resulting in correlation coefficients R^2 of 0.904 and 0.867 for the lower and higher load ranges, respectively. Values of interaction parameter α below 1 means that debonding initiates dominantly on the chord then stagnates and continues to grow on the brace, as can be seen in Fig. 15**.** For higher α values, R^2 value decreases and an α value above 1, i.e. α = 1.2, gives the lower R^2 values of 0.791 and 0.667 for the lower and higher load levels, respectively. The best fit interaction parameter is lower for the higher load range, showing that under the higher load range, debonding on the chord is more dominated during early cycles than that under the lower load range. The reason is the difference in strain energy release rate distribution on the braces and chord which will be shown in Section 5.

Based on the best α values obtained above, crack lengths on the braces obtained by the newly proposed method for different specimens are summarized and plotted against normalized number of cycles in Fig. 22. It can be seen from the figure that the crack propagates faster under the higher load range. The largest crack length on the brace under 15-165kN reaches above 200 mm at end of the test while under 10-110kN, the longest crack only reaches 60 mm. It can also be seen from the figure that for the same specimen, crack propagation rates on different braces are different, e.g. bottom brace of cX45-Ss-T_F3.1 has crack length of 200 mm in the end, while crack length on the top brace only reaches 80 mm. This difference in damage can also be reflected by Fig. 4. The reason could be different surface roughness of different steel braces as discussed in [10]. It should be noted that below 100 mm, the crack lengths on the braces are obtained with the influence of debonding on the chord, while above 100 mm, debonding on the braces is the predominate reason for strain increase on the surface so that the obtained crack lengths are more accurate.

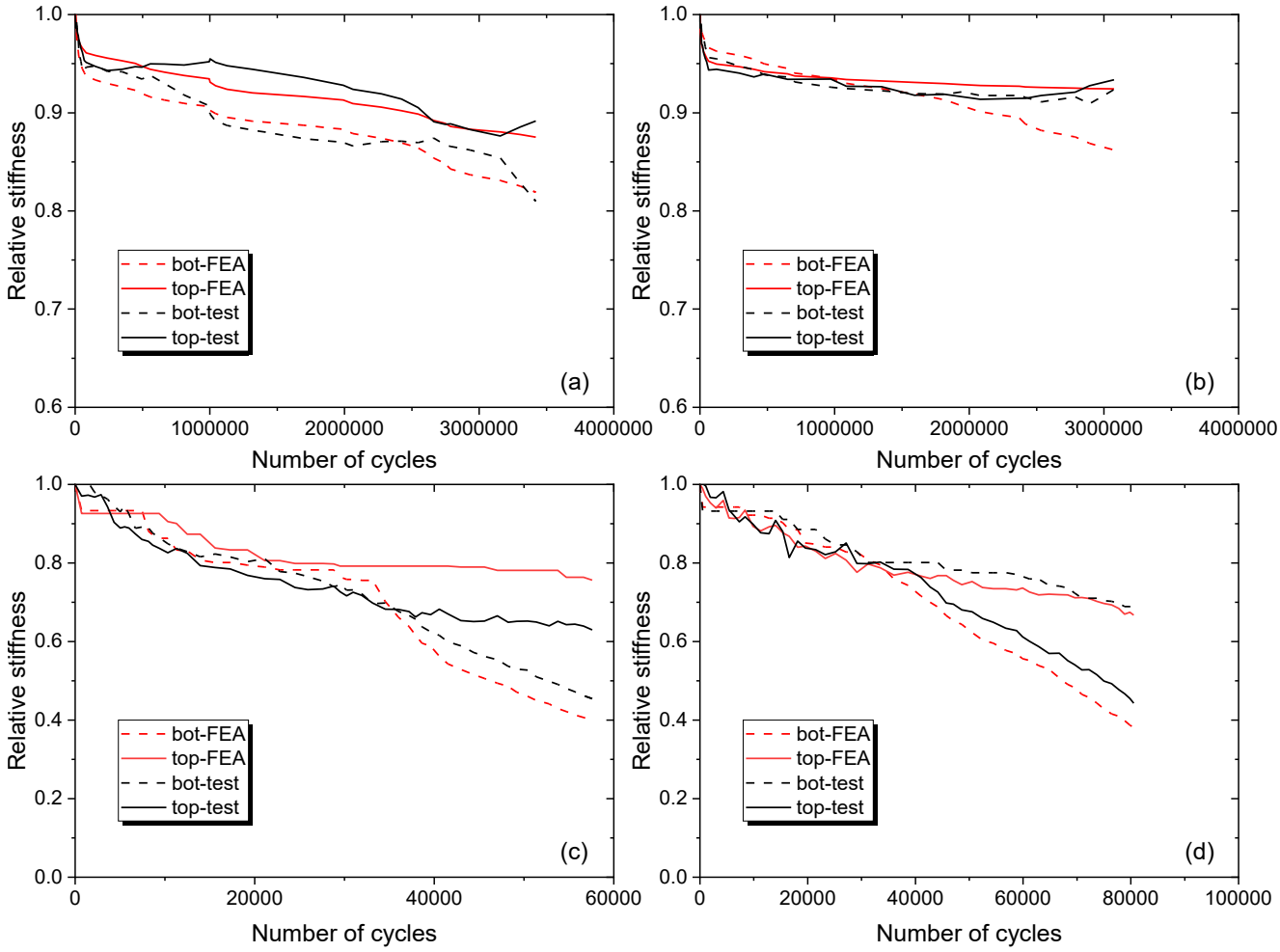

Fig. 23. Stiffness degradation curves: test (DIC + FEA) vs FEA results (a) cX45-Ss-T_F2.1; (b) cX45-Ss-T_F2.2; (c) cX45-Ss-T_F3.1; (d) cX45-Ss-T_F3.2.

Table 3
Comparison of final residual stiffness from FEA and test.

Load range (kN)	Specimens	Braces	Test (%)	FEA + test (%)	Difference (%)
10-110kN	cX45-Ss-T_F2.1	Top	89	88	−1.12
		Bottom	81	81	0.00
	cX45-Ss-T_F2.2	Top	93	92	−1.08
		Bottom	92	86	−6.52
15-165kN	cX45-Ss-T_F3.1	Top	63	75	19.05
		Bottom	45	40	−11.11
	cX45-Ss-T_F3.2	Top	44	38	−13.64
		Bottom	67	69	2.99

Based on the obtained crack lengths on braces and chords, stiffness degradation curves can be obtained by **Eq.** (4) and plotted versus test results in Fig. 23. It can be seen that the calculated stiffness matches very well with test results, indicating that the monitored crack lengths are accurate enough for further analysis. Table 3 compares the final stiffness degradation obtained from test and the calculated results in details. The difference between these two methods is within 15% except for the top brace of cX45-Ss-T_F3.1. It should be noted that the relationship between l_c and l_b defined in this paper can only be applied for this specific geometry of X45 joints. For other types of joints, e.g. joints with different angles, the relationship might be different and needs to be recalculated.

5. Discussion of FEA results

The most established assumption in the literature is that the crack propagation rate at the interface is governed by strain energy release rate (SERR) range at crack front according to Paris' law [41]. SERR range distributions at the crack fronts on the chord and the brace are shown in Fig. 24 under the high load range (15-165kN). All SERR distribution curves are smoothened which eliminates the influence of scatter of reading FE results on such complex crack front geometry. 4 stages of artificial crack development indicated by points A-D on the $\alpha = 0.2$ curve from Fig. 15 are selected here for detailed comparison and analysis. It should be noted that since there must be a pre-crack defined for the VCCT model, a small crack length of 2.83 mm on the brace, which equals to one element length, is assumed for the initial (point A) stage.

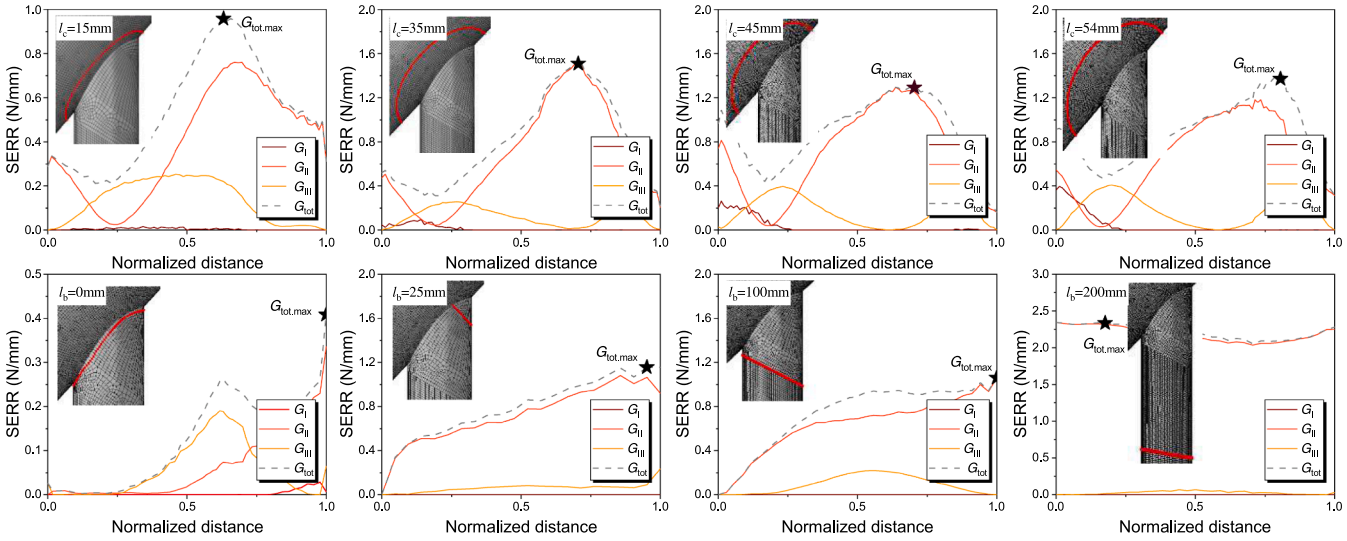

Fig. 24. SERR range distribution along crack fronts on chord and brace in function of crack length (load range 15-165kN).

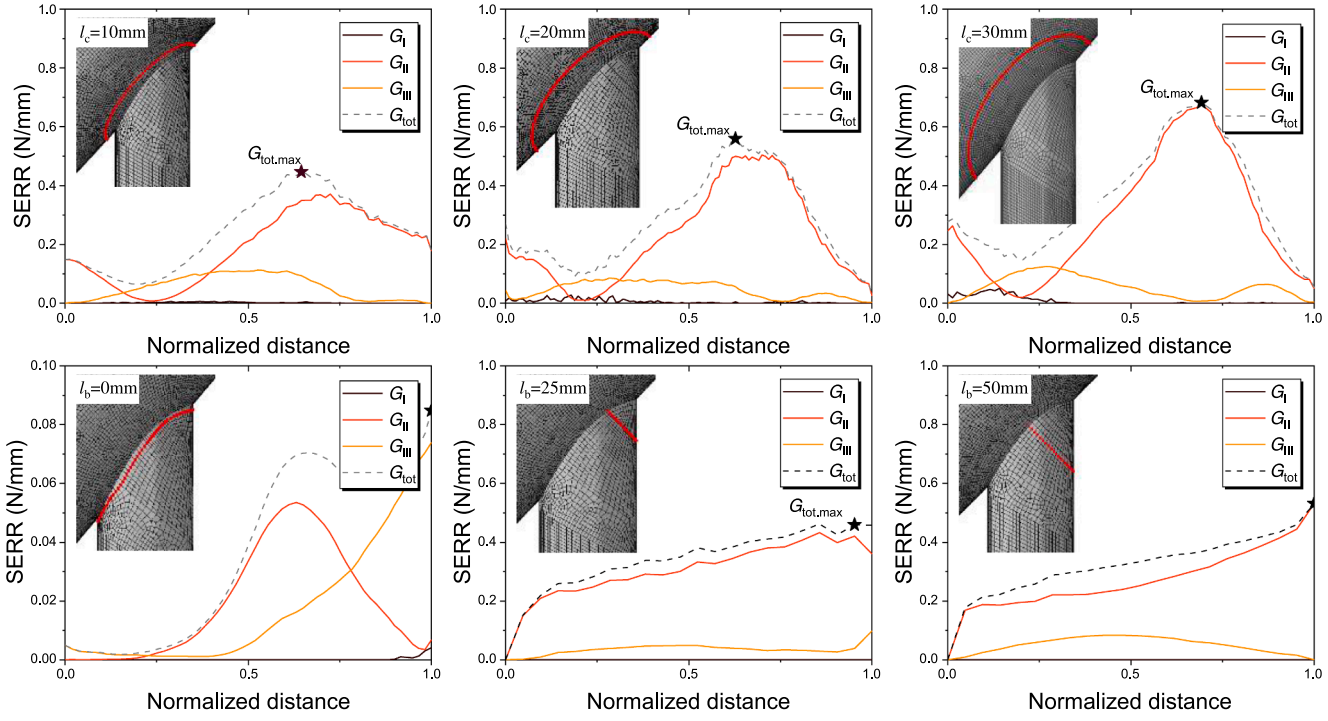

Fig. 25. SERR range distribution along crack fronts on chord and brace in function of crack length (load range 10-110kN).

The direction of normalized distance on the crack tip is indicated by arrows in Fig. 12. It can be seen from the figure that at initial stage (point A), the shear mode SERR, i.e. mode II and mode III SERR, dominate crack growth on the chord and brace. As the crack length develops, mode II debonding becomes more dominate, especially for the brace. Crack front on the chord indicates the maximum mode II SERR near the saddle point ranging from 0.8 to 1.6 N/mm. Mode I SERR is minimal along the whole crack front but increases a little bit near the crown heel at a later stage (point D) to 0.4 N/mm. This is because interface peel stress component resulting from the tensile load on the brace member becomes more obvious at crown heel than that at crown toe when the debonding on the chord becomes larger. The peak of SERR on the brace is mode II dominated near the crown toe with the value of 0.35 N/mm at initial stage. The distribution varies and the peak value is transferred to the crown heel and increases to value nearly 2.5 N/mm as the crack propagates. This explains why cracks on the brace initiates at obtuse corner but propagates more faster at the crown toe side, i.e. crack front becomes more perpendicular to the brace axis, at later stages. The peak value of mode II SERR on the chord is around 0.8 N/mm, larger than that on the brace (0.35 N/mm) at initial stage (point A in Fig. 15). As the crack propagates, peak values of mode II SERR on the chord increase up to 1.2 N/mm at point D while the same value on the brace increases to 2.5 N/mm. Such trend of SEER explains why debonding on the chord is dominant at initial stage (e.g. 10–20% of the fatigue life) followed by domination of debonding on the brace at the later stage.

Development of SERR range under 10-110kN load range is shown in Fig. 25, which has similar trend as that under the 15-165kN load range.

The total SERR range ΔG_{tot}, being summation of SERR for all 3 modes

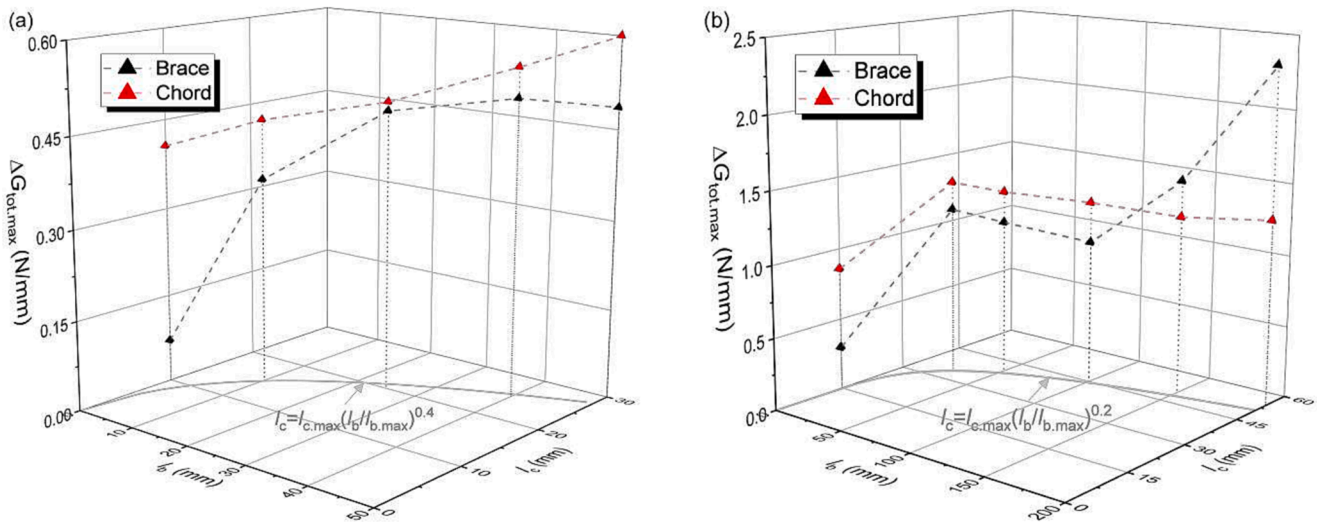

Fig. 26. Maximum total SERR range ($\Delta G_{tot.max}$) development on the chord and brace (a) under 10-110kN; (b) under 15-165kN.

separately, is a widely adopted similitude parameter for predicting the fatigue crack development under mixed-mode behaviour [42,43]. Hereby SERR ranges of different modes at crack tips in Fig. 24 and Fig. 25 are added together and ΔG_{tot} are obtained and plotted in the same figure (dashed line) for further analysis. The maximum values of ΔG_{tot} ($\Delta G_{tot.max}$) obtained along the analysed path are indicated with star on the total SERR curves and plotted separately in Fig. 26. The results are presented in function of crack lengths on the braces and chord assuming the best fit interaction of the two obtained previously in section 4.2. This interaction is visually presented by choosing the 3D plot that enables to indicate the considered crack lengths on the braces and chord, l_b and l_c, in the *x*-*y* plane. It can be seen that under 10-110kN, $\Delta G_{tot.max}$ on the chord is around 0.4 N/mm at initial stage, larger than that on the brace of 0.07 N/mm. At the later stage of crack progression, $\Delta G_{tot.max}$ on the brace and chord becomes similar. This explains very limited stiffness degradation (up to 10%) of the joint under lower load range as only the limited crack on the chord develops. Under 15-165kN load range, $\Delta G_{tot.max}$ on the chord is around 0.8 N/mm at initial stage while the same value on the brace is 0.3 N/mm. As the crack propagates, $\Delta G_{tot.max}$ on the brace increases to 2.4 N/mm while $\Delta G_{tot.max}$ on the chord remains below 1.5 N/mm. The higher $\Delta G_{tot.max}$ values on the chord at initial stage result in dominating failure mode as debonding on the chord for 15-165kN load range. As the $\Delta G_{tot.max}$ on the brace becomes lager at the later stages the dominating failure modes is debonding on the brace.

6. Conclusions

A combined DIC-FEA method for monitoring debonding crack propagation at the interface of bonded composite-to-steel joints is proposed in this paper. Core of the method is to use variation of strain distribution on surface of the bonded joint from DIC results to determine the debonding lengths at the interface under cyclic loading based on varied strain threshold values. A detailed FE model of the joint was built and validated against test results in terms of initial stiffness and strain distributions, which are then used for determining the strain threshold values as well as providing stiffness degradation laws versus crack lengths for validating the crack monitoring results. By modelling bond behaviour between composite and steel using VCCT, interaction of crack development on the braces and the chord is considered by comparing development of SERR values on the braces and chord, revealing the failure mechanisms of the joint. The method is applied to analyse fatigue tests of the wrapped composite joints with X geometry. These joints are characterized by complex 3D geometry (double curvature), non-uniform thickness of the composite wrap and interaction of the debonding crack propagation at the composite-to-steel interface on the braces and chord. The following specific conclusions can be drawn from analysis of the results at 2 different load ranges:

- Dominant failure mode is debonding on the brace which initiates at the root of braces and propagates towards the end of the composite wrap. Debonding on the chord interacts with debonding on the brace in the early stage of crack development.
- Under the high load range (15-165kN), debonding cracks on some of the braces develop to almost full wrapping length of 200 mm after 60,000 to 80,000 cycles, while others only reach 60–80 mm. This is thought to be due to different roughness of the steel tubes. Under the low load range (10-110kN), cracks on the braces reach only 20–60 mm, in combination with debonding on the chord, within 3 million cycles, corresponding to only 5–10% stiffness degradation of the joints in a non-critical failure mode.
- Interaction between debonding on the chord and on the brace, can effectively be assumed to follow a power-law-based relationship between crack lengths on the brace l_b and on the chord l_c with the power law parameter α. The best fitted α is found to be between 0.2 and 0.4 for the analysed high and low load ranges.
- Mode II behaviour is dominant for debonding on both chord and brace during the whole fatigue life, with the maximum SERR value existing at the saddle for the chord and at crown toes for the brace. The maximum total SERR range $\Delta G_{tot.max}$ is higher on the chord at initial stage but becomes lower than $\Delta G_{tot.max}$ on the brace at later stages, resulting in dominating failure mode as debonding on the chord at initial stage but transferring to the brace as the crack propagates.

CRediT authorship contribution statement

Weikang Feng: Investigation, Data curation, Writing – original draft, Visualization. **Pei He:** Investigation, Data curation, Visualization. **Marko Pavlovic:** Conceptualization, Methodology, Supervision, Writing – review & editing, Project administration, Funding acquisition.

Declaration of Competing Interest

The authors declare that they have no known competing financial interests or personal relationships that could have appeared to influence the work reported in this paper.

Acknowledgement

The authors are grateful to Dutch Research Council (NWO) for financially supporting the experiments presented in this paper through "Fatigue resistant Wrapped FRP Joints of Structural Hollow Sections" NWO Demonstrator 2018 project, grant No. 16949. The first author also would like to express his gratitude for the financial support from China Scholarship Council (CSC) under grant number of 201906260300.

Data availability

The raw/processed data required to reproduce these findings cannot be shared at this time as the data also forms part of an ongoing study.

References

[1] Wardenier J, Packer J, Zhao X. Vegte G van der. Hollow sections in structural applications. CIDECT 2010.
[2] Zhao XL, Zhang L. State-of-the-art review on FRP strengthened steel structures. Eng Struct 2007;29:1808–23. https://doi.org/10.1016/j.engstruct.2006.10.006.
[3] Jiao H, Zhao XL. CFRP strengthened butt-welded very high strength (VHS) circular steel tubes. Thin-Walled Struct 2004;42:963–78. https://doi.org/10.1016/j.tws.2004.03.003.
[4] Lesani M, Bahaari MR, Shokrieh MM. FRP wrapping for the rehabilitation of Circular Hollow Section (CHS) tubular steel connections. Thin-Walled Struct 2015;90:216–34. https://doi.org/10.1016/j.tws.2014.12.013.
[5] Fu Y, Tong L, He L, Zhao XL. Experimental and numerical investigation on behavior of CFRP-strengthened circular hollow section gap K-joints. Thin-Walled Struct 2016;102:80–97. https://doi.org/10.1016/j.tws.2016.01.020.
[6] Hu L, Feng P, Zhao XL. Fatigue design of CFRP strengthened steel members. Thin-Walled Struct 2017;119:482–98. https://doi.org/10.1016/j.tws.2017.06.029.
[7] Tong L, Xu G, Zhao X-L, Yan Y. Fatigue tests and design of CFRP-strengthened CHS gap K-joints. Thin-Walled Struct 2021;163:107694. https://doi.org/10.1016/j.tws.2021.107694.
[8] Pavlovic M, Bogers P, Veljkovic M. Method for making a virgin joint between two separate structural hollow sections, and such a virgin joint. US patent 2021;17/052:303.
[9] He P, Pavlovic M. Failure modes of bonded wrapped composite joints for steel circular hollow sections in ultimate load experiments. Eng Struct 2022;254:113799. https://doi.org/10.1016/j.engstruct.2021.113799.
[10] Feng W, Pavlovic M. Fatigue behaviour of non-welded wrapped composite joints for steel hollow sections in axial load experiments. Eng Struct 2021;249:113369. https://doi.org/10.1016/J.ENGSTRUCT.2021.113369.
[11] Iwashita K, Wu Z, Ishikawa T, Hamaguchi Y, Suzuki T. Bonding and debonding behavior of FRP sheets under fatigue loading. Adv Compos Mater 2007;16:31–44. https://doi.org/10.1163/156855107779755291.
[12] Min X, Zhang J, Wang C, Song S, Yang D. Experimental investigation of fatigue debonding growth in FRP - Concrete interface. Materials (Basel) 2020;13:1–18. https://doi.org/10.3390/ma13061459.
[13] Senthilkumar M, Sreekanth T, Reddy SM. Nondestructive health monitoring techniques for composite materials: a review. Polym Polym Compos 2021;29(5):528–40. https://doi.org/10.1177/0967391120921701.
[14] Duchene P, Chaki S, Ayadi A, Krawczak P. A review of non-destructive techniques used for mechanical damage assessment in polymer composites. J Mater Sci 2018 5311 2018;53:7915–38. 10.1007/S10853-018-2045-6.
[15] Ghiassi B, Verstrynge E, Lourenço PB, Oliveira DV. Characterization of debonding in FRP-strengthened masonry using the acoustic emission technique. Eng Struct 2014;66:24–34. https://doi.org/10.1016/j.engstruct.2014.01.050.
[16] Pohoryles DA, Melo J, Rossetto T, Fabian M, McCague C, Stavrianaki K, et al. Use of DIC and AE for monitoring effective strain and debonding in FRP and FRCM-retrofitted RC beams. J Compos Constr 2017;21(1). https://doi.org/10.1061/(ASCE)CC.1943-5614.0000715.
[17] Li J, Lu Y, Lee YF. Debonding detection in CFRP-reinforced steel structures using anti-symmetrical guided waves. Compos Struct 2020;253:112813. https://doi.org/10.1016/J.COMPSTRUCT.2020.112813.
[18] Yelve NP, Mitra M, Mujumdar PM. Detection of delamination in composite laminates using Lamb wave based nonlinear method. Compos Struct 2017;159:257–66. https://doi.org/10.1016/J.COMPSTRUCT.2016.09.073.
[19] Mustapha S, Ye L. Propagation behaviour of guided waves in tapered sandwich structures and debonding identification using time reversal. Wave Motion 2015;57:154–70. https://doi.org/10.1016/J.WAVEMOTI.2015.03.010.
[20] Ghosh KK, Karbhari VM. A critical review of infrared thermography as a method for non-destructive evaluation of FRP rehabilitated structures. Int J Mater Prod Technol 2006;25:241–66. https://doi.org/10.1504/IJMPT.2006.008882.
[21] Ghosh KK, Karbhari VM. Use of infrared thermography for quantitative non-destructive evaluation in FRP strengthened bridge systems. Mater Struct 2010 441 2010;44:169–85. 10.1617/S11527-010-9617-5.
[22] Owen RDB. Portable linear accelerators for X-ray and electron-beam applications in civil engineering. NDT E Int 1998;31:401–9. https://doi.org/10.1016/S0963-8695(98)00042-5.
[23] Lakshmi Aparna M, Chaitanya G, Srinivas K, Rao JA. Fatigue Testing of Continuous GFRP Composites Using Digital Image Correlation (DIC) Technique a Review. Mater Today Proc 2015;2:3125–31. https://doi.org/10.1016/J.MATPR.2015.07.275.
[24] Spiros Pantelakis P, Kadlec M, Kafka V. Strain concentration during the compression of a carbon/epoxy composite after impact. Int J Struct Integr 2015;6(2):279–89.
[25] Ghiassi B, Xavier J, Oliveira DV, Lourenço PB. Application of digital image correlation in investigating the bond between FRP and masonry. Compos Struct 2013;106:340–9. https://doi.org/10.1016/J.COMPSTRUCT.2013.06.024.
[26] Zhang P, Lei D, Ren Q, He J, Shen H, Yang Z. Experimental and numerical investigation of debonding process of the FRP plate-concrete interface. Constr Build Mater 2020;235:117457. https://doi.org/10.1016/J.CONBUILDMAT.2019.117457.
[27] Ali-Ahmad M, Subramaniam K, Ghosn M. Experimental Investigation and Fracture Analysis of Debonding between Concrete and FRP Sheets. J Eng Mech 2006;132:914–23. https://doi.org/10.1061/(ASCE)0733-9399(2006)132:9(914).
[28] Wang HT, Wu G, Pang YY, Shi JW, Zakari HM. Experimental study on the bond behavior between CFRP plates and steel substrates under fatigue loading. Compos Part B Eng 2019;176:107266. https://doi.org/10.1016/j.compositesb.2019.107266.
[29] Zheng B, Dawood M. Debonding of carbon fiber-reinforced polymer patches from cracked steel elements under fatigue loading. J Compos Constr 2016;20:04016038. https://doi.org/10.1061/(ASCE)CC.1943-5614.0000694.
[30] Szebényi G, Hliva V. Detection of Delamination in Polymer Composites by Digital Image Correlation—Experimental Test. Polymers (Basel) 2019;11:523. https://doi.org/10.3390/polym11030523.
[31] Ajmal OZ. The use of digital image correlation to monitor delaminations in composite structures. University of Surrey; 2018.
[32] Numerical Analysis and Modelling of Composite Materials. Springer Netherlands; 1996. 10.1007/978-94-011-0603-0.
[33] Pirondi A, Giuliese G, Moroni F. Development of a cohesive zone model for three-dimensional simulation of joint de-bonding/ delamination under mixed-mode I/II fatigue loading. Int J Struct Integr 2014;5:171–86. https://doi.org/10.1108/IJSI-02-2014-0008.
[34] Krueger R. Development of benchmark examples for static delamination propagation and fatigue growth predictions. Annu Forum Proc - AHS Int 2011;4:2593–616.
[35] Gliszczynski A, Wiącek N. Experimental and numerical benchmark study of mode II interlaminar fracture toughness of unidirectional GFRP laminates under shear loading using the end-notched flexure (ENF) test. Compos Struct 2021;258:113190. https://doi.org/10.1016/j.compstruct.2020.113190.
[36] Samborski S. Numerical analysis of the DCB test configuration applicability to mechanically coupled Fiber Reinforced Laminated Composite beams. Compos Struct 2016;152:477–87. https://doi.org/10.1016/j.compstruct.2016.05.060.
[37] Abaqus 6.14 Documentation n.d. http://130.149.89.49:2080/v6.14/ (accessed September 22, 2021).
[38] Teimouri F, Heidari-Rarani M, Haji AF. An XFEM-VCCT coupled approach for modeling mode I fatigue delamination in composite laminates under high cycle loading. Eng Fract Mech 2021;249:107760. https://doi.org/10.1016/j.engfracmech.2021.107760.
[39] Liu Y, Lemanski S, Zhang X, Ayre D, Nezhad HY. A finite element study of fatigue crack propagation in single lap bonded joint with process-induced disbond. Int J Adhes Adhes 2018;87:164–72. https://doi.org/10.1016/J.IJADHADH.2018.10.005.
[40] MATLAB - MathWorks - MATLAB & Simulink n.d. https://nl.mathworks.com/products/matlab.html (accessed August 25, 2021).
[41] Anderson WE, McEvily AJ. Discussion: "A Critical Analysis of Crack Propagation Laws" (Paris, P., and Erdogan, F., 1963, ASME J. Basic Eng., 85, pp. 528–533). J Basic Eng 1963;85:533–533. 10.1115/1.3656901.
[42] Quaresimin M, Ricotta M. Fatigue behaviour and damage evolution of single lap bonded joints in composite material. Compos Sci Technol 2006;66:176–87. https://doi.org/10.1016/J.COMPSCITECH.2005.04.026.
[43] Bernasconi A, Jamil A, Moroni F, Pirondi A. A study on fatigue crack propagation in thick composite adhesively bonded joints. Int J Fatigue 2013;50:18–25. https://doi.org/10.1016/J.IJFATIGUE.2012.05.018.